Phase diagram of crystals of dusty plasma

H. C. Lee* and D. Y. Chen
Department of Physics, National Central University, Chungli, Taiwan 320, Republic of China
and Center for Complex Systems, National Central University, Chungli, Taiwan 320, Republic of China

B. Rosenstein†
Department of Electrophysics, National Chiao-Tung University, Hsinchu, Taiwan, Republic of China
(Received 18 February 1997)

Dust particles effectively charged by plasma recently have been optically observed to exhibit crystalline phases not expected of Wigner or Yukawa crystals. Under varying conditions the crystal sometimes appears as deformed and oriented three-dimensional close-packed lattices of bcc, fcc, or hcp type, but mostly as a triangular array of vertical chains of particles. The unusual phases are shown to be caused by dipole-dipole interactions. The dipole moments are induced on the dust particles by gravity and by drag forces generated by ion stream. We describe in detail stable lattice structures and present the highly complex phase diagram of the dusty plasma. It turns out that in large parts of the phase diagram the stable phases indeed correspond to chains, but particles in neighboring chains belong to different sublattices. The stability of the lattices against excitations due to compression (i.e., aspect ratio variations) and vibration (i.e., phonons or charge density waves) is established. [S1063-651X(97)07409-6]

PACS number(s): 52.90.+z, 61.66.−f, 64.70.−p

I. INTRODUCTION

A rather surprising recent experimental observation of stable ordered structures of dust particles in plasma [1–7] opened the possibility to study Wigner-type crystals and their direct melting on the ''microscopic'' level using simple optical microscopy. The stability of these structures in a volatile plasma environment is due to very effective charging of the particles, so that Coulomb interactions become much stronger than what is needed to overcome the thermal motion. In most experiments, especially when the dust particles are large (radius exceeds a few μm), one observes a triangular two-dimensional (2D) lattice repeated many times (in some experiments, however, only few times) in the vertical direction [2–4] that is similar to an Abrikosov flux-line lattice in type II superconductors.

However, different crystal structures were also observed in the experiment with the most genuinely three-dimensional sample [1]. Some cubic bcc- and fcc-like structures are reminiscent of the phases of the classical Wigner crystal. Closer examination shows that these cubic crystals have preferred orientations. In this case, as in the colloidal suspension, which has somewhat similar properties [8,9], the Coulomb interaction is screened and becomes a Yukawa potential. Yet another observed structure is of hcp type, which lies intermediate between the cubic close-packed and the loosely packed ''2D'' structures. This structure is normally unstable in systems with Coulomb [10] and Yukawa [9] interactions although in these cases its energy is only slightly higher than those of the cubic ones. It appears to be stable in quite large portions of the observed dusty plasma phase diagram [11]. In sum, an obvious difference in the crystal structure of the dust particles from Wigner or Yukawa crystals is the dominance in the former of the 2D triangular structure and to a lesser degree the hcp-like structure and the preferred orienations of the cubic structures.

It is quite clear to what additional external forces this difference should be attributed. First there is gravity, which is no longer negligible in these systems. The direction of the lines in the triangular phase is not random as in the case of a normal spontaneous breaking of the full, continuous rotational symmetry—it always points down [12]. Another possible source is the drag force exerted on the dust particles by the ion stream in the plasma [13]. Recent Monte Carlo simulations of limit-size [14] and two-layer [15] systems that took into account the effects of gravity and ion stream demonstrated that dust particles indeed could crystallize in the vertical direction. Gravity and the drag forces balance the electric force that keeps the dust particles afloat. As a consequence, the particles (in the bulk of the dusty plasma away from confining side walls), in addition to their negative charge [16,17], have dipole moments oriented along the z direction induced by the electric force [18]. The moments add a repulsive force in the horizontal x and y directions and an attractive force in the vertical z direction. This imbalance, which is enhanced by the screening effect, creates vertical lines of dust particles.

In this paper we report on a theoretical study of the phase diagram of plasma crystals. While molecular dynamics simulation [13–15] has been very useful for studying the interaction between individual particles, it is not practical for large lattices. The situation is similar to that in condensed matter physics. There quantum mechanics is used to study the effective interactions between ions but classical summation of energy over a chosen lattice structure is used to study the properties of large systems. Following this analogy, we study the *macroscopic* phase diagram of the dusty plasma crystals by comparing the summed energies of the system placed on a variety of lattices. The interaction among the dust particles is the dominant monopole-monopole (Yukawa) interaction

*Electronic address: hclee@halley.phy.ncu.edu.tw
†Electronic address: baruch@phys.nthu.edu.tw

modified by an effective dipole-dipole interaction that accounts for the actions of the microscopic gravity and drag forces. To our knowledge this is the first study of this kind for dusty plasma crystals.

We show that, under conditions that appear to be consistent with the experiments, a dipole-dipole interaction as weak as that which may be induced by gravity alone already plays a decisive role in the phase diagram. At first sight it may seem surprising that gravity could have such an effect on a structure mainly dictated by electromagnetism. This turns out to be the combined effect of several causes: the size of the mesoscopic dust particles is just about right for gravity to begin to compete with electromagnetism; near stability the energy difference between different crystal structures typically is just a minute fraction of the potential energy; Debye screening enhances the effect of dipole-dipole interaction. The demand for accuracy is reflected in the size of the lattice used in the computation, which is typically $30/a$ cubed, where a is the lattice spacing in units of the Debye length. This accuracy requirement makes molecular dynamics simulation untenable for $a<4$. As we shall see, the most interesting part of the phase diagram lies in the region $1\leqslant a\leqslant 6$.

The dipole-dipole interaction, which breaks rotational invariance, is induced by the drag force as well as by gravity but, owing to large theoretical and experimental uncertainties, it is not clear which (or if either) one of them is the dominant agent. This is discussed in Sec. II. At the end of this paper, Sec. VIII, we propose an experiment to discriminate between the two possibilities.

The presence of dipole-dipole interactions makes the phase diagram very complicated, perhaps comparable to that of liquid crystals, since dust particles become similar to oriented ''molecules.'' This makes it necessary to classify the crystalline phases, which is done in Sec. III. Owing to the directional nature of the dipole-dipole interaction discussed above, the lattice initially responds to it by flattening in the z direction followed by adjustments of the aspect ratio in the x-y plane. Therefore, it is not sufficient, say, to just describe the phases as ''elongated bcc (or fcc),'' as is done in some experimental papers, since there are several nonequivalent ways to squeeze bcc, and there are phases that cannot be simply obtained by squeezing. We base the classification on the remaining symmetries.

We numerically calculate and compare the energies of possible crystalline structures at zero temperature in Sec. IV. The calculation is supported by an analytical one presented in the Appendix, where we expand in the small parameter D, the ratio of the relative strength of the dipole-dipole interaction to that of the monopole-monopole interaction. The result is the phase diagram Fig. 1. At very small dipole moments, when the system approaches the well studied Yukawa lattice, the slightly flattened bcc and fcc are the stable modes. At slightly larger moments various orientations of bcc and fcc become distinguishable. At still larger moments the flattening in the z direction and adjustments of the aspect ratio in the x-y plane become appreciable, so that in some cases the favored lattices should be classified as orthorhombic. For relatively large moments the phase diagram is occupied by the triangular (at smaller a) and orthorhombic lattices.

In Sec. V we check the stability of the states found in the last section by studying excitations of the crystals, namely, the charge-density sound waves. In practice, we compute dispersion relations for the excitations. Thermal excitations are introduced next in Sec. VI, where the finite temperature mean-field formalism is briefly reviewed. We use the Lindemann criterion to map the melting line. The phase diagram for finite temperature (i.e., room temperature) is shown in Fig. 4, where, for the purpose of connecting with experiment, the results are presented using the electron density and dust particle density as coordinates. It turns out that the phases cannot be discussed in terms of only the three-dimensional Bravais lattice types; the symmetry is lower. As a result some transitions between deformed bcc and fcc are not phase transitions but rather crossovers. Transitions among triangular, rhombic, and liquid are, however, always genuine first order phase transitions. Owing to the fact that the dusty plasma system is not generally in a state of perfect thermal equilibrium and the energies of different crystalline structures are close, some phases can coexist, a phenomenon that seems to have been observed in some experiments. Section VIII contains concluding remarks.

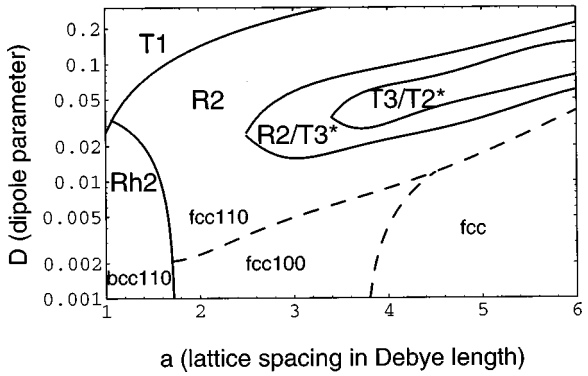

FIG. 1. Phase diagram plotted as a function of the dipole parameter D and the lattice spacing a at zero temperature. Solid lines separate different crystalline phases and dashed lines indicate crossovers. Bold letters indicate different crystal structures, whose related squeezed 3D lattices are indicated by lower case letters and numerals giving the direction of the squeeze.

II. PARAMETERS AND FORCES IN DUSTY PLASMA

There are many parameters that describe the states of dusty plasma. Only three dimensionless combinations of these parameters—D, a, and T^*, respectively the relative (dimensionless) strength of the dipole-dipole interaction, the lattice spacing, the temperature—are relevant for the determination of the phase structure. These parameters are defined below.

The basic force between (the dust) particles is the screened Coulomb repulsion. The charge Q on particles in dusty plasma experiments is rather large, $\sim 10^3-10^5$ electron charges according to various estimates. In what follows we use natural units with $4\pi\epsilon_0=1$; this implies that $e^2\ \mu\mathrm{m}^{-1}=1.4\times10^{-3}\ \mathrm{eV}=2.3\times10^{-22}\ \mathrm{J}$. A very simple estimate is

$$Q=C\Delta\phi\approx 4\pi\epsilon_0 r_P\Delta\phi, \tag{1}$$

where C is the capacitance of, basically, a sphere of radius r_P. The radius varies from a fraction of μm to tens of μm.

The potential difference $\Delta\phi$ between the surface of the particle and the plasma is obtained [16] by equating the thermal electron current towards the dust particle,

$$I_e = \pi r_P^2 n_e \sqrt{\frac{8kT_e}{\pi m_e}} \exp \frac{e\Delta\phi}{kT_e} \tag{2}$$

to the ion current,

$$I_i = \pi r_P^2 n_i \sqrt{\frac{8kT_i}{\pi m_i}} \left(1 - \frac{e\Delta\phi}{kT_i}\right). \tag{3}$$

Here e is the electron charge, m, T, and n are mass, temperature, and particle density, and the subscripts e and i denote electron and ion, respectively. The electron energy distribution is usually not the equilibrium one; the distribution is peaked at a few eV. The ion temperature T_i is about the same as room temperature. The density n_e, an important control parameter which depends on the rf power, is approximately equal to the density of ions and is of order 10^9-10^{10} cm^{-3}. These formulas (1)–(3) were found to be not very accurate in experiment [4] and might overestimate the charge. More accurate estimates can be made by solving Poisson-Vlasov equations under certain assumptions [17] or obtained from independent experiments [4].

At distances large enough compared to particles size r_P, the Coulomb force in the plasma is effectively screened to become a Yukawa potential whose range is given by the Debye length λ,

$$\frac{1}{\lambda} = \sqrt{\frac{e^2}{4\pi\epsilon_0}\left(\frac{n_e}{kT_e} + \frac{n_i}{kT_i}\right)} \approx \sqrt{\frac{n_i e^2}{4\pi\epsilon_0 kT_i}}. \tag{4}$$

This estimate can be improved [17]. The important fact is that in all plasma crystal experiments the interparticle distance $\overline{a} \equiv 1/n_P^{1/3}$, with the particle density n_P being of order 10^4-10^5 cm^{-3}, is a few tens to hundreds of μm and is larger than λ.

We will use λ as the unit of length and $Q^2/4\pi\epsilon_0\lambda$ as the unit of energy. In these units $a \equiv \overline{a}/\lambda$ is a number varying from about 1 to 10. The dusty plasma therefore resembles a hard-sphere system or a metal more than it resembles a classical unscreened Coulomb system.

We assume that the particles reach thermal equilibrium with the ions and neutral atoms at room temperature and ignore the fact that at very large distances the potential decays even faster than Yukawa. Following conventions adopted in the colloidal suspensions theory, we will frequently use a dimensionless ''scaled temperature'' $T^* \equiv kT/V(a)$, where $V(r)$ is the Coulomb potential in our units:

$$V(r) = \exp(-r)/r. \tag{5}$$

A distinctive feature of the plasma crystals is that the gravity force on the relatively heavy dust particles cannot be neglected even when compared to the strong electrostatic forces. For a particle to be suspended in the bulk of the crystal, an overall approximately constant electric field E should balance the gravity and the drag force caused by the ion stream [19]:

$$Mg + F_{\text{drag}} = QE, \tag{6}$$

where $M = (4\pi/3)r_P^3\rho$ is the mass of a spherical particle with density ρ. The combined electric, gravitational, and drag forces will keep the center of gravity of the particle at rest, leaving the electric field to induce an electric dipole moment on the charge distribution on the particle. The mechanism of how the electric field induces dipole moments on particles in the plasma was carefully discussed in [18]. A simple approximate expression for the dipole moment, with P the polarizability, is

$$d = PE = 4\pi\epsilon_0 r_P^3 E. \tag{7}$$

Now we calculate the interaction between two particles carrying both charge and a dipole moment. Given two distributions of charge $\rho_1(\vec{s})$ and $\rho_2(\vec{s}')$ centered around $\vec{r}$ and $\vec{r}'$, respectively, and interacting through v, one has

$$\begin{aligned} v(\vec{r}-\vec{r}') &= \int_{\vec{s}}\int_{\vec{s}'} \rho(\vec{s}) V(\vec{s}-\vec{s}') \rho(\vec{s}') \\ &= Q_1 Q_2 V(\vec{r}-\vec{r}') + (Q_2\vec{d}_1 - Q_1\vec{d}_2)\cdot\vec{\nabla}_{\vec{r}} V(\vec{r}-\vec{r}') \\ &\quad - (\vec{d}_1\cdot\vec{\nabla}_{\vec{r}})(\vec{d}_2\cdot\vec{\nabla}_{\vec{r}}) V(\vec{r}-\vec{r}'), \end{aligned} \tag{8}$$

where $V(\vec{s}-\vec{s}')$ has been expanded around $\vec{r}-\vec{r}'$ to $O(\vec{s}-\vec{r})$ and $O(\vec{s}'-\vec{r}')$, and Q_i and $\vec{d}_i$ are the charge and electric dipoles:

$$Q_1 = \int_{\vec{s}} \rho_1(\vec{s}), \quad Q_2 = \int_{\vec{s}'} \rho_2(\vec{s}'),$$

$$\vec{d}_1 = \int_{\vec{s}} (\vec{s}-\vec{r})\rho_1(\vec{s}), \quad \vec{d}_2 = \int_{\vec{s}'} (\vec{s}'-\vec{r}')\rho_2(\vec{s}'). \tag{9}$$

Equation (8) shows that the dipoles enter the picture via interactions of dipole-monopole and dipole-dipole type. In a region where all the particles have the same charge and dipole moment the monopole-dipole interactions cancel exactly. In the present study we shall focus on such a case and also ignore finite size effects, which is justified since the ratio of particle size to lattice spacing, $r_P/(a\lambda)$, is much less than unity. Then the major effect on the crystal structure produced by dipoles is the screened dipole-dipole interaction and the two-particle interaction simplifies to

$$v(\vec{r}-\vec{r}') = Q^2 V(\vec{r}-\vec{r}') - d^2 \frac{\partial^2}{\partial z^2} V(\vec{r}-\vec{r}'). \tag{10}$$

Using the simplified notation $V(r)$ for $V(\vec{r})$, we write in our energy and length units the interaction at $\vec{r}' = \vec{0}$ as

$$v(\vec{r}) = V(r) + U(r,z) \tag{11}$$

with the dipole-dipole interaction being

$$U(r,z) = -D\frac{\partial^2}{\partial z^2}V(r)$$
$$= -D[z^2(1/r^3+3/r^4+3/r^5)-1/r^2-1/r^3]e^{-r}, \tag{12}$$

where D is a dimensionless strength of the dipole-dipole interaction. An examination of Eq. (12) reveals that U is attractive between two nearest neighbors in the z direction and repulsive in the x-y plane. For $r>1$, which is true when the interparticle distance is greater than the Debye length, the leading terms, those proportional to z^2/r^3 and $(3z^2-r^2)/r^4$, come from screening, as compared with the Columbic term $1/r^3$. That is, the effect of the dipole-dipole interaction is enhanced by screening.

In the case of $F_{\rm drag}=0$, D has the form

$$D=\frac{d^2}{Q^2\lambda^2}\approx\left[\frac{4\pi r_p^6\rho g e}{3Q^2}\right]^2\frac{4\pi\epsilon_0 n_e}{kT_i}\equiv n_e V_D. \tag{13}$$

Here the volume V_D is defined to highlight the dependence of D on n_e. This rough estimate brings out an important point: D grows very rapidly, certainly faster than Q does, with increasing r_p. The drag force is difficult to estimate quantitatively [13,14]. In what follows we will not discuss it explicitly except to point out that the effect of its presence is to increase the value of D. With the drag force ignored, the set of values $n_e=10^9$ cm^{-3}, $r_p=5$ μm, $\rho=3$ g cm^{-3}, $Q=1000$, $kT_i=300$ K yields $D=0.0042$. Typical experimental values [1–4] suggest that D ranges from <0.001 to a few times 0.1. It will be shown that the phase of the dusty plasma is effected when D is as small as 0.001, and that triangular phases begin to occur within the range $D\sim 0.02-0.1$. The mesoscopic size of $r_p\approx 5$ μm seems to be just right for the interface of gravity with electromagnetism to be interesting.

III. CLASSIFICATION OF LATTICES

Since the dipole-dipole interaction is attractive in the z direction and repulsive in the x-y plane, it will generally flatten the lattices. Hence a crystal will no longer be invariant under rotations that are not around the z axis. This implies, for instance, that two relatively rotated bcc crystals could deform differently under the influence of the dipole-dipole interaction. In fact, as will be discussed in detail below, we find a proliferation of crystal structures as soon as the dipole-dipole interaction is turned on. In the experimental papers the crystals were characterized using the 3D Bravais lattices oriented in different ways with respect to the z axis. With the 3D rotational symmetry having been explicitly broken by gravity and the drag force, we classify the crystal structure according to the remaining symmetry: the 2D x-y plane rotations and translations in the plane as well as along the z direction. These crystals, which are either vertically twofold or threefold symmetric layers of regular two-dimensional sublattices in the x-y plane, are sometimes recognizable as slightly deformed versions of rotated bcc and fcc and of hcp along a specific symmetry axis when D is small, but not necessarily so when D is not small.

Of the regular two-dimensional Bravais lattices, we find that the triangular lattice is extremely robust whereas the rectangular and rhombic ones are relatively malleable. We classify stable crystals into classes (2D Bravais)n, where n is the number of horizontally shifted sublattices that are of the same Bravais type. In our calculation five categories appear on the phase diagram: Rh2, $R2$, $T1$, $T2$, and $T3$, where Rh, R, and T stand for rhombic, rectangular, and triangular, respectively. Tn with $n>3$ and Rn and Rhn with $n\neq 2$ are energetically not competitive within the range of parameter values we considered.

The simplest lattice, the hexagonal crystal $T1$, is stable where D is large. In the $n=2$ or $n=3$ cases there are some aspect ratios of the lattice that need optimization. For Rh2 and $R2$, a lattice site of a sublattice is vertically aligned with the centers of the faces of the sublattices just above and just below it. We denote by a_x and a_y, $a_x\leqslant a_y$, the two lattice spacings in the x-y plane, and define the in-plane aspect ratio $g_\parallel=a_x/a_y$. For $T2$ and $T3$ we denote the lattice spacing in the horizontal by a_t. In all cases, we denote by a_z the vertical spacing between repeated sublattices and define the vertical aspect ratio $g_\perp=a_x/a_z$. We now describe the lattices in more detail.

A. $R2$

The unit cell of the two-dimensional sublattice is rectangular. The volume per particle is

$$\rho^{-1}=a_x a_y a_z/4=a_x^3/2g_\parallel g_\perp. \tag{14}$$

The coordinates of the lattice sites on the two sublattices in units of a_x are

$$(x,y,z)=\left(l,\frac{m}{g_\parallel},\frac{k}{g_\perp}\right),$$
$$(x',y',z')=\left[l+\frac{1}{2},\left(m+\frac{1}{2}\right)\frac{1}{g_\parallel},\left(k+\frac{1}{2}\right)\frac{1}{g_\perp}\right], \tag{15}$$

where l, m, and k are integers. Some crystals belonging to this class are given in the table below:

	bcc (100)	fcc (100)	fcc (110)	rcp
$g_\parallel$	1	1	$1/\sqrt{2}$	$1/\sqrt{3}$
$g_\perp$	1	$1/\sqrt{2}$	1	

where fcc (110), say, means the regular fcc crystal with the (110) vector pointing in the z direction. The crystal denoted rcp is not a regular lattice, rather it is obtained by splitting a regular two-dimensional triangular into two rectangular sublattices by pushing down every other lattice site. This means that the views of rcp and $T1$ (see below) from directly above are identical.

B. Rh2

We consider a subclass of rhombic lattices sometimes called oblique. The unit cell of the two-dimensional sublat-

tice is a regular diamond. Note that Rh2 and $R2$ coincide when the diamond is a square, namely, when $g_{\|}=1$. The volume per particle is

$$\rho^{-1}=a_x a_y a_z/4=a_x^3/4g_{\|}g_{\perp}. \tag{16}$$

The coordinates of the lattice sites on the two sublattices in units of a_x are

$$\begin{aligned}(x,y,z)&=\left(l+\frac{m}{2},\frac{m}{2g_{\|}},\frac{k}{g_{\perp}}\right),\\ (x',y',z')&=\left[l+\frac{m}{2}+\frac{1}{2},\frac{m}{2g_{\|}},\left(k+\frac{1}{2}\right)\frac{1}{g_{\perp}}\right],\end{aligned} \tag{17}$$

where l, m, and k are integers. Some crystals belonging to this class are given in the table below

	bcc (100)	bcc (110)	fcc (100)
$g_{\|}$	1	$1/\sqrt{2}$	1
$g_{\perp}$	$\sqrt{2}$	$1/\sqrt{2}$	1

Note that fcc (110) and bcc (100) both belong to $R2$ and Rh2 and therefore have a higher symmetry then either bcc (110) and fcc (100).

C. $T1$

The unit cell of the two-dimensional sublattice is a triangular. Our computation confirms that the equilateral triangular is extremely robust against deformation. So only one lattice length, a_t, is needed in the x-y plane. The volume per particle is

$$\rho^{-1}=\sqrt{3}a_t^2 a_z/2=\sqrt{3}a_t^3/2g_{\perp}. \tag{18}$$

The coordinates of the lattice sites on the single sublattices in units of a_t are

$$(x,y,z)=\left(l+\frac{m}{2},\frac{\sqrt{3}}{2}m,\frac{k}{g_{\perp}}\right). \tag{19}$$

D. $T2$

The robustness of the equilateral triangular implies that only one lattice length, a_t, is needed in the x-y plane. The volume per particle is

$$\rho^{-1}=\sqrt{3}a_t^2 a_z/4=\sqrt{3}a_t^3/4g_{\perp}. \tag{20}$$

The coordinates of the lattice sites on the two sublattices in units of a_t are

$$\begin{aligned}(x,y,z)&=\left(l+\frac{m}{2},\frac{\sqrt{3}}{2}m,\frac{k}{g_{\perp}}\right),\\ (x',y',z')&=\left[l+\frac{m}{2},\frac{\sqrt{3}}{2}\left(m+\frac{2}{3}\right),\left(k+\frac{1}{2}\right)\frac{1}{g_{\perp}}\right].\end{aligned} \tag{21}$$

A regular crystal belonging to this class is the hexagonal closed-packed crystal hcp, whose aspect ratio is $g_{\perp}=\sqrt{8/3}$.

E. $T3$

Symmetry in the z direction means that there is only one spacing between sublattices. The volume per particle is

$$\rho^{-1}=a_t^2 a_z/2\sqrt{3}=a_t^3/2\sqrt{3}g_{\perp}. \tag{22}$$

The coordinates of the lattice sites on the three sublattices in units of a_t are

$$\begin{aligned}(x,y,z)&=\left(l+\frac{m}{2},\frac{\sqrt{3}}{2}m,\frac{k}{g_{\perp}}\right),\\ (x',y',z')&=\left[l+\frac{m}{2},\frac{\sqrt{3}}{2}\left(m+\frac{2}{3}\right),\left(k+\frac{1}{3}\right)\frac{1}{g_{\perp}}\right],\\ (x'',y'',z'')&=\left[l+\frac{m}{2},\frac{\sqrt{3}}{2}\left(m-\frac{2}{3}\right),\left(k-\frac{1}{3}\right)\frac{1}{g_{\perp}}\right].\end{aligned} \tag{23}$$

A regular crystal belonging to this class is fcc (111), whose aspect ratio is $g_{\perp}=1/\sqrt{6}$. Note that the particle densities of hcp and fcc (111) are identical.

IV. ZERO TEMPERATURE

We start with the phase diagram at zero temperature. In this case the energy per particle is just

$$\frac{1}{2}\epsilon(g)\equiv\frac{1}{2}\sum_{\mu\neq 0}v(\vec{R}_{\mu}), \tag{24}$$

where $v(\vec{r})=V(r)+U(r,z)$ is the interaction given in Eq. (11), μ denotes a lattice site, and $\vec{R}_{\mu}$ is its position relative to the origin $\vec{R}_0=0$. The summation is over lattice sites excluding the origin. Since $\vec{R}_{\mu}$ depends on the aspect ratios $g_{\perp}$ and $g_{\|}$ (in the case of Tn, only on $g_{\perp}$), which we collectively call g, these quantities are implicit functions of g. At zero temperature the ground state energy per particle is just $\epsilon(g)$.

An example of the energy $\epsilon(g)$ plotted against g_z and g_y for $R2$ at $a=4$ and $D=0.3$ is shown in Fig. 2, where equienergy contours are given upside down, and a locally stable configuration is shown as a maximum. The two highest peaks in Fig. 2 refer to the same lattice related to each other by the exchange of the coordinates x and y.

In Fig. 1 the phase diagram is given as a function of D and a at zero temperature. Here as well as in what follows, unless explicitly stated, optimization with respect to g is understood. The well-known bcc-fcc transition at $a=1.73$ [9,20,21] is indicated, although even for D as small as 0.001 there are already preferred orientations. For $a>4$ the dipole effect is so weak that the various orientations of the fcc lattice are practically degenerate with $D<0.01$, beyond which the phase diagram becomes more complex. As the lattices become increasingly deformed by the dipole interactions, it becomes necessary to label the (deformed) bcc (110) lattice as Rh2, fcc (110) as $R2$, fcc (111) as $T3$, and so on. For Rh2, the effect of deformation on the aspect ratios never exceeds a few percent. For $R2$ the effect can be large. For example, for $a=2$, $(g_{\|},g_{\perp})$ is (0.697, 1.04) at $D=0.02$ and it is (0.607, 1.30) at $D=0.1$. In the phase diagram * is used to indicate the phase with a close second lowest energy. There is a

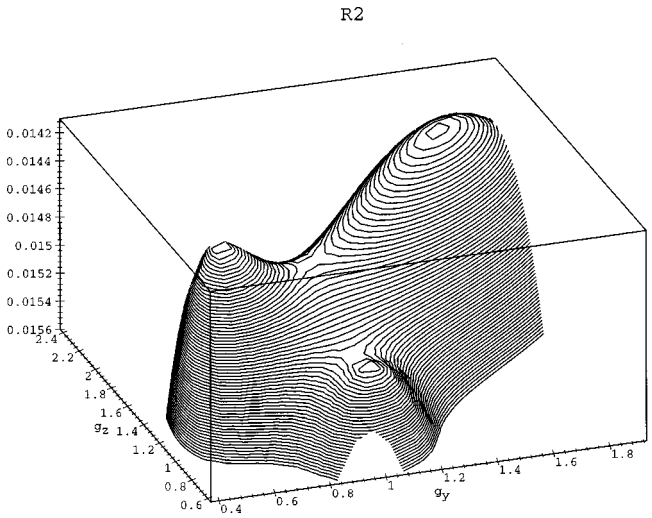

FIG. 2. Zero-temperature equienergy contours for the $a=4$ $R2$ lattice plotted against the two aspect ratios $g_y=g_\parallel$ and $g_z=g_\perp$, at $D=0.3$. The picture is turned upside down to display the locally stable points, which appear as maxima, more clearly. The two degenerate maxima, which describe the same crystal related by interchange of x and y, is connected by a saddle point in the middle. A third local minimum in the foreground represents an unstable crystal structure.

narrow strip in the upper-right corner of Fig. 1 where $T3$ is stable and where $T2$ is almost degenerate with $T3$ (energies are within one part in 10^5) and a larger strip where $T3$ is almost degenerate with $R2$. When uncertainties or distributions in the values of the parameters of the system is taken into account, one expects the $R2$, $T2$, and $T3$ to coexist in the general area.

The phase diagram is dominated by $R2$ and $T1$ above the line $D\approx -0.024+0.054a$. When D is greater than the critical value given by $D_c=-0.861+0.111a+0.0128a^2$, indicated by the $R2\rightarrow T1$ transition line in Fig. 1, $g_\parallel$ for R2 takes the critical value $\sqrt{1/3}$ (at this value the 2D projections of $R2$ and $T1$ are identical) and $R2$ and $T1$ simultaneously collapse vertically to become the same 2D hexagonal lattice *within our model*, where the dust particles are represented by points. In practice, two particles are strongly repulsed by the unscreened Coulomb force when they are separated by less than one Debye length. Therefore when a lattice vertically collapses in our model, we take it to indicate that the actual vertical separation of the horizontal two-dimensional sublattice is about one Debye length, regardless of the value of a. We call this a ''collapsed'' $T1$ state; it occupies the upper left-hand corner of Fig. 1. The critical value for vertical aspect ratio is $g_\perp\approx 2.177-0.112a$. These features are not much changed at finite temperature.

The numerical results for small D are verified by an analytical calculation in the Appendix, where we use the small D expansion to examine how some three-dimensional lattices respond to the presence of a small dipole-dipole force.

To summarize, at zero temperature the phase diagram contains a multitude of different crystal structures. Real experiments are, however, conducted when the dust particle system is kept roughly at room temperature (although thermal equilibrium might be far from perfect). In this case there is one more phase—a liquid phase—and a more refined methods should be used. We first study excitations at zero temperature before returning to this in Sec. VI.

V. EXCITATIONS IN PLASMA CRYSTALS

For small deviations from the three-dimensional Yukawa crystal, caused by the presence of a small dipole force (i.e., small D), one expects the dust particles to crystallize to the usual close-packed three-dimensional symmetric lattice, with a small amount of squeezing that can be determined by perturbation theory. Even then there are various possible orientations of the lattice to consider before squeezing. At larger D the dust particle system is rather unusual, and it is no longer evident that any crystalline structure will be formed. In other words, it is not clear that the crystalline structures whose energies we calculated in the last section are indeed stable. In this section we consider small vibrations of the plasma crystals around a specific crystal structure. Dispersion relations including sound velocities are presented. The vibrations are just those of the usual sound waves (we assume there is only one kind of particle), which, because the particles are charged, are charge-density waves too. It is possible that these waves can be generated and observed optically. They interact among themselves, with lattice defects and with other excitations in plasma. For the present work, we use the dispersion relations to check the stability of those crystal structures whose binding energies we compute using methods described in the last section and as a guide to find other possible stable lattices.

By a stable crystal structure we mean that there is no other structure *with the same symmetry* that has a lower energy. This is the case when all the harmonic excitations have real positive frequencies $\omega(\vec{k})$ where $\vec{k}$ runs over the whole Brillouin zone of the lattice. For Wigner crystals this kind of check was first performed by Foldy [22].

The formalism to calculate the dispersion relation in harmonic approximation is well known [22]; we just quote the form used in numerical simulations. For the wave vector $\vec{k}$, the polarization vectors $u^i(\vec{k})$ and $\omega(\vec{k})^2$ are eigenvectors and eigenvalues of the matrix

$$D^{ij}(\vec{k})=\frac{1}{M}\sum_{\mu\neq 0}\left[1-\cos(\vec{k}\cdot\vec{R}_\mu)\right]\left.\frac{\partial^2 v(r)}{\partial r^i\partial r^j}\right|_{\vec{r}=\vec{R}_\mu}. \quad (25)$$

Here M is the mass of the dust particle and the summation extends over all lattice sites R_μ except the origin.

We performed the stability check for the standard Wigner crystal lattices and found that, for every lattice, as D exceeds a certain value, unstable modes $\omega(\vec{k})^2<0$ appear for some orientation of the wave vector and some polarization. This information is used to guess the preferred deformation(s) of crystal structure. The instability of the original lattice is further verified by the fact that the energy of a new (i.e., deformed) lattice, optimized with respect to aspect ratio(s), has a lower energy. The stability of the new lattices is also tested by computing their sound modes. It should be pointed out that this method can only be used to test local stabilty, and only among lattices with the same symmetry.

An example of the dispersion relations for a stable and an unstable configuration of a $R2$ lattice is shown on Fig. 3,

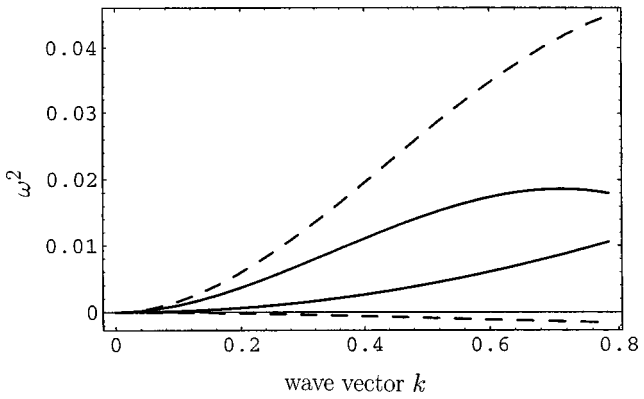

FIG. 3. Dispersion relations for the stable configuration (''solid lines'') and saddle point configuration (''dashed line'') of Fig. 2. For each case and corresponding to each value of the wave number two eigenvalues ω^2—one for transversal wave vector and one longitudinal wave vector—are shown. For the stable configuration ω^2 is always real and positive, whereas the unstable saddle point configuration has negative modes.

where equienergy contours are given as a function of $g_\perp$ and $g_\parallel$. Only dispersion curves in one direction of propagation $(1,\sqrt{3},0)$ in the x-y plane are plotted. Solid lines correspond to two eigenvalues of ω^2 of the stable point (near peak in Fig. 2; the far peak represents the same lattice) at $g_\perp=1.2918$ and $g_\parallel=0.61265$, while the two dashed lines correspond to those of the unstable saddle point at $g_\perp=1, g_\parallel=1.53$. The longitudinal branch has by far the larger frequencies (sound velocities for small k), while transversal waves have very small frequencies. One can clearly see that one branch of the unstable lattice has negative ω^2. Similar analysis verifies that the phases given in Fig. 4 are at least locally stable.

VI. FINITE TEMPERATURE EFFECTS AND MELTING

At zero D the finite temperature phase diagram has been extensively studied using several different methods. The first, analytical mean-field type calculation [9,20] is the simplest and physically most easily understandable method. It

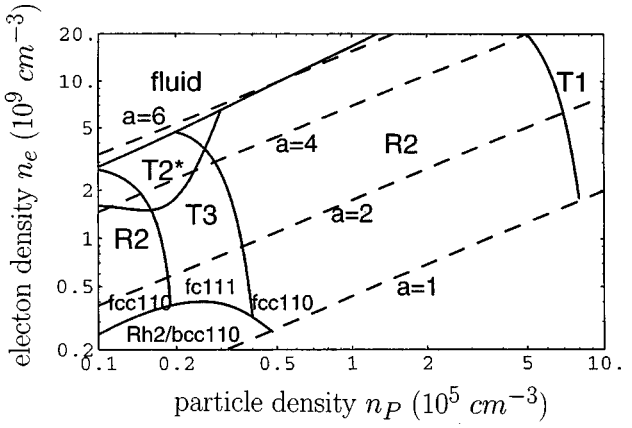

FIG. 4. Phase diagram plotted against electron density n_e and particle density n_P for $V_D=2\times10^{11}$ cm^3, which corresponds to $D\approx0.02n_e/10^9$ cm^{-3}. Temperature is fixed at room temperature and dashed lines are lines of constant lattice spacing.

usually assumes the Einstein approximation for the phonon spectrum (although [20] went beyond it) and the harmonic approximation (see, however, calculation of anharmonicity effects in [9]). This method provides a general picture of the phase diagram, namely, that at some critical temperature the bcc or fcc crystal melts into a liquid.

The second is molecular dynamics and Monte Carlo simulations [21,23,24]. Interestingly, for the Yukawa potential, there were significant quantitative differences between the simple mean-field theory and the simulation results, which apparently stabilized after initial controversy [25]. The main difference concerns the value of the coefficient c_L in the so-called Lindermann criterion that phenomenologically well describes the solid-liquid phase transition line:

$$\langle \Delta x^2 \rangle = c_L^2 a^2. \tag{26}$$

It turns out that Δx^2 is underestimated by the mean-field approach owing to possible neglect of large contributions from some low frequency modes [20]. However, it was noted in [20] that the molecular dynamics melting line (as, for example, for hard spheres) can be well reproduced if in the mean-field theory a smaller value for the effective Lindermann constant is used.

The exact shape of the bcc-fcc transition line near melting is an extremely delicate issue already at $D=0$, because within a sizeable range of the parameters the energies of the two crystals are very close to each other. The mean-field theory [9] fails to detect the improved stability of bcc compared to fcc at these temperatures found in simulations. Nothing essential is changed in this respect when nonzero D is introduced.

The third method employs a more complicated density functional theory, which was applied to the Yukawa system after the simulation results became available [26]. Although this method usually gives results closer to those obtained by numerical simulation, its interpretation is not so transparent. In rotationally nonsymmetric cases the method becomes much more complicated to apply and the interpretation of its result even less transparent.

Our numerical results do not have a level of accuracy needed to resolve the above mentioned issue in the case of nonzero D. Hence a sophisticated treatment for finding the exact location of the melting line is not warrented and we shall use the far simpler mean-field approach and apply the Lindermann criterion to determine the melting line. This means that our result near the melting line is less precise than in other parts of the phase diagram.

The description of the method is found in the literature [9,20]. The main point is to allow Gaussian deviations around each site R_μ on the lattice, which comes down to replacing a function $O(R_\mu)$ by the Gaussian averaged

$$\langle O(R_\mu)\rangle = \int \prod_{i=1}^{3} \left[\frac{dx_i'}{(2\pi)^{1/2}\xi_i} \exp\left(-\frac{x_i'^2}{2\xi_i^2} \right) \right] O(R_\mu - \vec{r}'), \tag{27}$$

where $x_1=x$, $x_2=y$, $x_3=z$, and $\xi_i=\xi_{x_i}$ are the mean deviations. The potential energy at a point $\vec{r}$ near the lattice site R_0 taken as the origin is then

$$\langle e(\vec{r})\rangle = \sum_{\mu\neq 0}\langle v(\vec{R}_\mu-\vec{r})\rangle$$
$$= \sum_{\mu\neq 0}\int\prod_{i=1}^{3}\left[\frac{dx_i'}{(2\pi)^{1/2}\xi_i}\exp\left(-\frac{x_i'^2}{2\xi_i^2}\right)\right]v(\vec{R}_\mu-\vec{r}-\vec{r}')$$
$$= \sum_{\mu\neq 0}\int\prod_{i=1}^{3}\left[\frac{dx_i'}{(2\pi)^{1/2}\xi_i}\left(v(\vec{R}_\mu)+\sum_j\frac{1}{2}(x_j+\tilde{x}_j)^2\frac{\partial^2}{\partial x_j^2}v(\vec{R}_\mu)\right)\right]+O(\xi^3,r^{-3})$$
$$= \epsilon+\frac{1}{2}\sum_i[(\xi_i^2+x_i^2)\Sigma_i]. \quad (28)$$

Here $v(\vec{r})=V(r)+U(r,z)$ is the interaction given in Eq. (11) and ϵ and Σ_i, whose dependence on g is not made explicit, are the lattice sums,

$$\epsilon\equiv\sum_{\mu\neq 0}v(\vec{R}_\mu),\quad \Sigma_i\equiv\sum_{\mu\neq 0}v''_{x_ix_i}(\vec{R}_\mu),\quad i=1,2,3. \quad (29)$$

Note that $V(r)$ has the property $\nabla^2V(r)=0$ and the $i\neq j$ terms in Eq. (28) cancel upon lattice summation. The free energy per particle is approximated by

$$F=-T\ln\left(\int d^3r\,\exp[-\beta\langle e(r)\rangle]\right)-\frac{1}{2}\langle e(0)\rangle, \quad (30)$$

while ξ_i^2 is identified to this order with $\langle\Delta x_i^2\rangle$:

$$\xi_i^2=\langle\Delta x_i^2\rangle$$
$$=\left(\int d^3r x_i^2\,\exp[-\beta\langle e(r)\rangle]\right)\times\left(\int d^3r\,\exp[-\beta\langle e(r)\rangle]\right)^{-1}. \quad (31)$$

This yields the self-consistent relations

$$\xi_i^2\Sigma_i=T \quad (32)$$

and the free energy for a given aspect ratio g [recall that g stands for the set of aspect ratio(s) specifying a lattice]

$$F=\frac{1}{2}\left(\epsilon(g)+\frac{3}{2}T\right)-\frac{T}{2}\sum_{i=1}^{3}\ln\frac{2\pi T}{\Sigma_i}. \quad (33)$$

The final value of the free energy taken is that minimized with respect to g.

In practice, the minimum set of summed lattice sites is dictated by the numerical accuracy required. An accuracy of five to six significant figures is needed to determine the relative stability of, say, bcc and fcc lattices if an accuracy of 0.05 is required in a. Achieving such an accuracy calls for a summation of all sites within a radius of approximately 15 Debye lengths. For $a=1$ this implies a $30\times30\times30$ lattice that needs to be summed over. Since the dipole potential is proportional to the second derivative of a Yukawa function, a computation of high accuracy at small a becomes quite lengthy when $D\neq0$, as it involves the fourth derivatives of a large sum of Yukawa functions. For this reason we do not consider cases with $a<1$, which, as mentioned earlier, in any case is in a region for which the model is not reliable.

From Eqs. (26) and (32), the Lindermann criterion for the melting temperature is

$$T_m=c_L^2a^2\Sigma_z. \quad (34)$$

It turns out that in order to reproduce the melting line obtained in Monte Carlo simulations for the $D=0$ case we need $c_L^{\rm eff}\approx0.054$. That this value is so small compared with the value derived from Monte Carlo simulation simply reaffirms the known fact that the mean-field approximation is not the best method for studying melting—many soft modes not considered in the method have a small effect on the energy but has a large influence on the melting. Since the dependence of the free energy on T is weak compared to its dependence on D, we adopt the above value for $c_L^{\rm eff}$ universally. Then in all cases the solid to liquid curve is approximately given by the line $T_m^*\approx0.04a-0.03$, where $T^*=kT/V(a)$ is a universal dimensionless scaled temperature.

VII. PHASE DIAGRAM OF THE DUSTY PLASMA AND RESULTS

In experiments certain parameters such as the rf power are varied while others are kept fixed. In particular the dust particle temperature is fixed at $T=T_i=300$ K. To roughly simulate a laboratory setting, we take $V_D=2\times10^{11}$ cm^3 and let $n_{e0}\equiv n_e/10^9$ cm^{-3} and $n_{p0}\equiv n_P/10^5$ cm^{-3} range from 0.2 to 20 and 0.1 to 10, respectively. Then $D\approx0.02n_{e0}$, $\lambda_0\approx(2/n_{e0})^{1/2}$, $a\approx1.52n_{e0}^{1/2}n_{P0}^{-1/3}$, and the dimensionless temperature $T^*\approx4.31\times10^{-4}n_{P0}^{-1/3}e^a$.

The calculated phase diagram is shown in Fig. 4 in a $\log n_P$ $\log n_e$ plot. No result is given for $a<1$ where the model is not reliable.

In Fig. 4 the melting line almost coincides with the $a=6$ line and is approximately given by $T_m^*=0.2$. In terms of the dimensionless coupling strength $\Gamma=Q^2V(r_0/\lambda)/(4\pi\epsilon_0r_0kT)$, where $r_0=(3/4\pi n_P)^{1/3}$ is the Wigner-Seitz radius of the dust particles, the melting temperature corresponds to a strength of $\Gamma_m\approx70\pm10$, similar to the value ≈67 obtained in [20] for colloidal suspensions. In a typical experiment [1], n_P is fixed and n_e is varied indirectly by varying the rf power. The phase diagram indicates that turning up the rf power, which will cause n_e to increase, will eventually cause melting. This seems to agree with experiment [1]. Note that even as T is kept unchanged, increasing n_e increases λ and consequently T^*.

The phase diagram in the region $n_{P0}\leqslant0.5$ is quite complex, with four lattices occupying five domains. Whereas transitions such as $R2\rightarrow T3$ are real phase transitions, changes such as bcc $(110)\rightarrow$Rh2 and fcc $(110)\rightarrow R2$ are crossovers. It is explained in the Appendix that $R2\rightarrow$Rh2 appear as first order transitions, but on a finer scale are also crossovers. Strictly speaking, there is a second order phase transition whenever fcc bifurcates to two oriented fcc-type lattices. As complex as it has made the phase diagram in this region, the dipole interaction changes the aspect ratio from

its $D=0$ value by less than 4%. In the domain marked by $T2^*$, $T2$ has the second lowest energy, but its energy is greater than the energies of the stable phases by less than a few parts in 10^5. In fact, in this region the energies of Rh2, $R2$, $T3$, and $T2$ are all within a fraction of 10^{-4} of each other. Given that the experimental values of n_e and n_P have a non-negligible spread, we expect these phases to coexist in a typical experimental setting.

The region $0.5 \geqslant n_{P0} \geqslant 6$ is dominated by $R2$, whose energy is lower than those of $T2$ and $T3$ by more than 0.03% when $n_{P0} > 2$. Here $R2$ typically has aspect ratios ($0.58 \geqslant g_\parallel \geqslant 0.68$, $1.1 \leqslant g_\perp \leqslant 1.5$) that render it no longer recognizable as a deformation of fcc (110). The upper right-hand corner of the phase diagram is occupied by the collapsed $T1$ state explained earlier, which typically has $g_\perp \geqslant 1.7$. In comparison, our computation shows that a quasi-2D lattice of several layers (not surprisingly) may have uncollapsed stable $T1$ structure. In particular, with 5 layers, the phase diagram in the region $2 \leqslant a \leqslant 4$ is occupied by $T1$ with $1.5 \geqslant g_\perp \geqslant 1.2$, and in the region $4 < a \leqslant 6$ has two phases, $R2$ below the line $D \approx 0.616 - 0.271/(a-3.6)$ and $T1$ above and along which $1.2 \geqslant g_\perp \geqslant 1.6$ for $T1$.

VIII. CONCLUDING REMARKS

In summary, our study suggests that induced electric dipole interaction, whose strength is a rapidly increasing function of the dust particle size, can explain the crystalline phases of dusty plasma seen in experiments. Debye screening enhances the effect of the dipole-dipole interaction. The presence of the dipole interaction is first manifest in the preferred orientation of the cubic lattices. At intermediate dipole strength, the triangular lattices $T3$ and $T2$ [deformed fcc (111) and hcp, respectively] begin to coexist with the preferred cubic lattice $R2$ [fcc (110)]. At higher dipole strength the vertically collapsed hexagonal $T1$ is the stable phase. In this case it would be appropriate to discribe the dust particle system as a triangular array of vertical chains of particles. Aside from the simple existence of stable triangular phases, our calculation also shows that even lattices that look three dimensional are squeezed and usaully have preferred orientations. The aspect ratios differ by up to 10% from the 3D values. This effect should be optically measurable.

The question remains as to whether gravity or the drag force is mainly responsible for the dipole moment. At the moment this question cannot be experimentally clearly resolved because in all the experiments reported so far the direction of gravity coincides with that of the ion stream. It seems that in an experiment in which the chamber holding the plasma is tilted, thereby making the directions of the two forces different, one would be able to disentangle effects of the two forces.

In this study we have left out several effects that could be important. One is the finite size effect: the number of layers in the z direction in some experiments is quite small and the total number of dust particles moving coherently in the dusty plasma may be of order 1000 or much smaller. In this case one can employ the finite size scaling analysis such as that described in [21]. We also assumed that the size of the dust particles is uniform throughout the plasma, which may not be true. Since the dipole is extremely sensitive to the particle size, a small distribution in particle size may be sufficient to smear of even alter the transition line we have calculated. If particle size and dipole are not uniform over the lattice, then monopole-dipole interactions cannot be ignored. The inclusion of this interaction may have a significant effect on the phase diagram, and may explain why in our phase diagram the $T1$ phase is not as preponderant as some experiments suggest. On the other hand, our calculation also shows that the $T1$ phase easily dominates when the sample is only several layers thick. In any case the consequence of the presence of the monopole-dipole interaction should be looked into. In using the mean-field approximation we ignored the effect of soft phonon modes, which is abound in the plasma environment. For this we paid the price by using a very small value for the Lindermann coefficient.

ACKNOWLEDGMENTS

The authors are grateful to Professor I. Lin for discussions. This work was supported in part by Grant Nos. 85-2112-M-008-017 (H.C.L.) and 86-2112-M-009-034 (B.R.) from the National Science Council, ROC.

APPENDIX: PERTURBATION THEORY IN D

In this Appendix we calculate energies of some lattices using small D perturbation theory. For simplicity we impose the condition $g_\parallel = 1$, and write $g_\perp$ as g and allow it to vary. This restricted breaking of the symmetry already gives an indication of how the complexity of the phase diagram grows by the increase of an extra degree of freedom.

The zero's order is the Yukawa crystal results. These are the usual 3D lattices. The value of unperturbed aspect ratio g_0 is determined by symmetry to be 1, 1, and $\sqrt{2/3}$ for B, F, and H, standing for bcc, fcc, and hcp respectively. In the case of triangular, symmetry, T does not dictate a value for g_0 but our computation shows it to be ≈ 1.07. In the following, we refer to a generic lattice spacing a for all lattices as $a^3 \equiv a_P^2 b_P$. The number of particles in a unit volume a^3 is 2, 4, $4/\sqrt{3}$, and $2/\sqrt{3}$ for B, F, H, and T, respectively.

Here it is worthwhile pointing out that g facilitates a smooth interpolation between B and F: when fcc (100) is flattened by increasing g from 1 to $\sqrt{2}$ a regular bcc (100) is obtained. Similarly, when bcc (100) is elongated by decreasing g from 1 to $1/\sqrt{2}$, a regular fcc (100) is obtained.(See tables for $R2$ and Rh2 in Sec. III.) Therefore, given the g degree of freedom, the change from phase F to phase B is strictly not a phase transition, but a crossover. The energy ϵ is implicitly a function of a, g, and D. For fixed a and D, g is determined by minimizing ϵ. Without the dipoles, $g = g_0$ and the energy depends solely on a, in which case it is well known that there are only two stable lattice structures: B for $a < 1.72$ and F for $a > 1.72$. The third close-packed 3D structure, H, has a slightly higher energy. In the presence of dipoles the value of g will increase from g_0.

For $D > 0$, the F-B crossover point is only slightly larger than the $D=0$ critical value of $a = 1.72$. A curious observation is that the full symmetry of the B lattice is restored at some point as a passes through a B-F crossover point. This

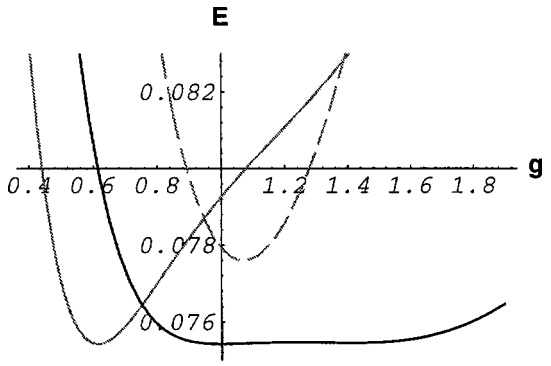

FIG. 5. Energies per particles as a function of aspect ratio $g=g_\perp$ for three different lattices: F (black line), H (gray), and T (dashed gray). The lattice spacing $(1/n_P^3)$ is $a=3$. $g_\parallel$ is fixed at 1. The B lattice is not shown since it overlaps with F on the present scale.

can be understood in terms of two facts: (a) at full symmetry B (at $g=1$) is equivalent to a very flattened F (at $g=\sqrt{2}$); and (b) when $D>0$ all stable lattices are flattened. Suppose at some $D>0$ the crossover point is $a=a_0$. Let us consider the transition from (a flattened) F [fcc (110)] to a flattened B [bcc (100)] as a passes through a_0. When $a<a_0$, a flattened B is stable and $g>\sqrt{2}$. At $a>a_0$, a flattened F is stable. Thus, as a passes through a_0 from above, F becomes increasingly flat and g passes through $\sqrt{2}$ from below to reach a value greater than $\sqrt{2}$. At some value of a, g must be equal to $\sqrt{2}$, which corresponds to the perfect bcc (100) lattice. This is not a stable B lattice, however, since a stable B is flattened and must have $\sqrt{2}>g>1$. In practice, the transition

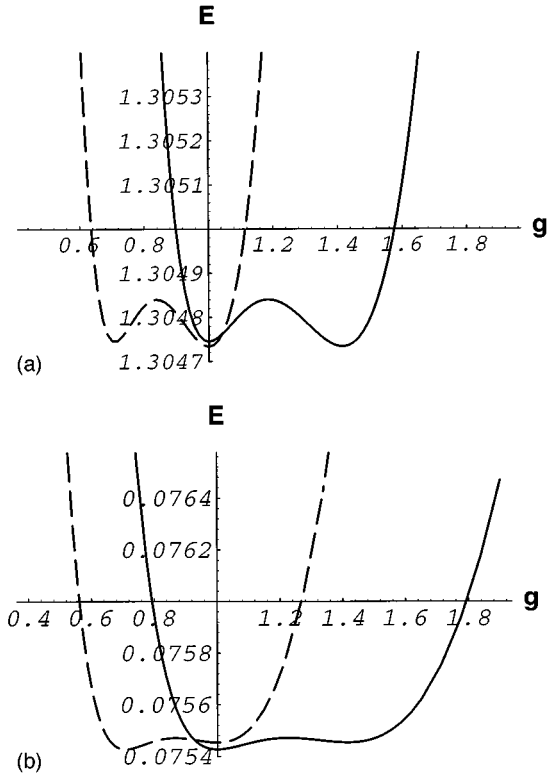

FIG. 6. Energies per particles as function of aspect ratio $g=g_\perp$ for B (dashed line) and F (solid line) lattices for (a) $a=1.5$ and (b) $a=3$. $g_\parallel$ is fixed at 1.

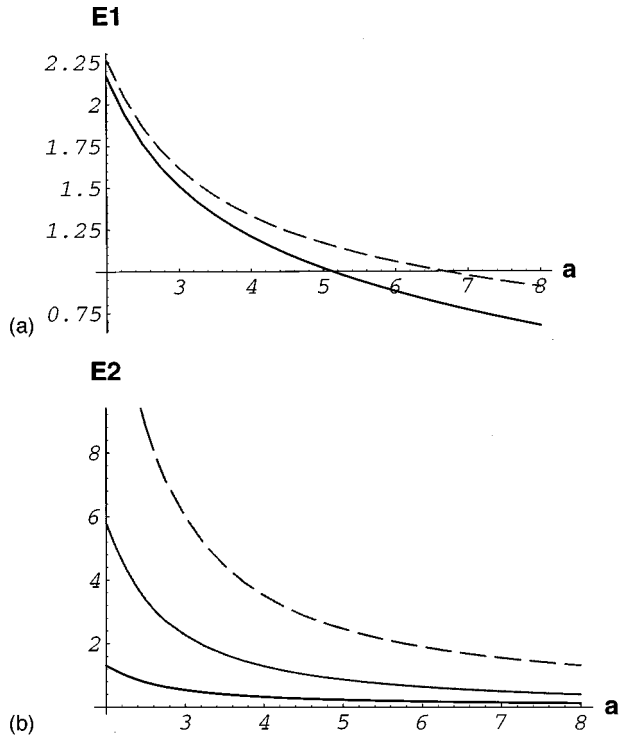

FIG. 7. Energies per particles as a function of lattice spacing a for T (dashed gray), H (gray), and F (black), in perturbation theory in D. All the energies are scaled with $V(a)$. (a) The leading coefficient for T and F. The coefficient for H practically coincides with that for F on the present scale. (b) Coefficient of the next to leading term for the three lattices.

happens very quickly: g goes rapidly from slightly greater than 1 to slightly greater than $\sqrt{2}$ in a small interval centered at $a=a_0$. Thus the crossover *appears* as a first order transition.

The D dependence enters the expression for the energy per particle in two ways. First, there is the dipole-dipole interaction term proportional to D:

$$\epsilon(g,a)=e(g,a)-Dw(g,a) \tag{A1}$$

and, second, the value of g is shifted:

$$g=g_0+g_1D+O(D^2). \tag{A2}$$

A typical dependence of energy per particle e of various lattices at $D=0$ on the aspect ratio is shown in Fig. 5 for the case $a=3$. One can see that the triangular lattices T (dashed gray line) and H (gray) each has a sharp minimum at their respective g_0, while the cubic F (black) has a very wide flat section between $g\approx 1$ and $g=\sqrt{2}$. On a finer scale, Fig. 6(a), this flat plateau resolves into a global minimum at $g_F=g_0=1$ and a local one at $g_F=\sqrt{2}$. The B lattice, not shown in Fig. 5 (since the B and F plateaus on that scale are indistinguishable) is also shown in Fig. 6(a) (dashed black line). One sees that its local minimum at $g_B=1$ is higher

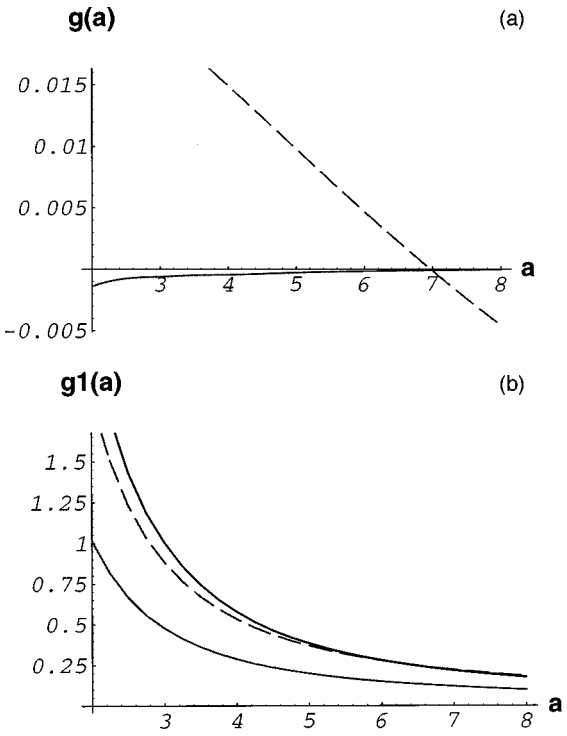

FIG. 8. Aspect ratio $g=g_\perp$ as a function of lattice spacing a for T (dashed gray), H (gray), and F (black), in perturbation theory in D; $g_\parallel$ is fixed at 1. (a) The $D=0$ values for the triangular lattices T and H. (b) The next to leading term for the three lattices.

than the local minimum of F and the global minimum at $g_B=1/\sqrt{2}$ coincides with F's global minimum. In fact at the global minima the lattices are equivalent and relatively rotated versions of the regular F. Below the phase transition point $a=1.72$ the roles of the global and local minima are interchanged. Figure 6(b) shows the result for $a=1.5$. Here the global minimum of B at $g_B=g_0=1$ coincides with the global minimum of F at $g_F=\sqrt{2}$. They are equivalent and relatively rotated versions of the regular B.

In any case one can approximate the energy per particle as a function of g in the neighborhood of the global minimum g_0 by a parabola:

$$e(g)=e(g_0)+\frac{1}{2}\frac{\partial^2}{\partial g}e\Big|_{g=g_0}(g-g_0)^2+O(\Delta g^3)$$

$$\equiv e_0+\frac{1}{2}e_2\Delta g^2+O(\Delta g^3). \tag{A3}$$

This correction starts therefore from second order in D. As we will see shortly, the leading order correction in D is not sufficient to account for peculiarities of the phase transitions. To second order in D, one has to expand the dipole-dipole term to first order in Δg:

$$w(g)=w(g_0)+\frac{\partial}{\partial g}w(g)\Big|_{g=g_0}\Delta g\equiv w_0+w_1\Delta g. \tag{A4}$$

The correction to the aspect ratio found from minimizing ϵ is therefore

$$\Delta g=D\frac{w_1}{e_2}+O(D^2) \tag{A5}$$

and the energy is

$$\epsilon=e_0-Dw_0-D^2\frac{w_1^2}{2e_2}+O(D^3). \tag{A6}$$

In Figs. 7(a) and 7(b) the first and second corrections to the energy per particle divided by $V(a)$ as functions of a are plotted. Solid line denotes F, gray line H, and gray dashed line T. In Fig. 7(a) H is not shown because it virtually coincides with F. So the only conclusion one can draw from this order is that at sufficiently large D, T becomes stable against both close-packed lattices. The competition between F and H is decided by the second order effect [Fig. 7(b)]: H is stable at intermediate values of D. We see that H and even more so T can better take advantage of the dipole-dipole interaction. Similarly Figs. 8(a) and 8(b) provide leading and correction terms for the aspect ratio.

[1] J. H. Chu and Lin I, Phys. Rev. Lett. **72**, 4009 (1994); Lin I, C.-H. Chiang, J. H. Chu, and W.-T. Jaun, Chin. J. Phys. **33**, 453 (1995).
[2] Y. Hayashi and K. Tachibana, Jpn. J. Appl. Phys., Part 1 **33**, 804 (1994).
[3] H. Thomas, G. E. Morfill, V. Demmel, J. Goree, B. Feuerbacher, and D. Mohlmann, Phys. Rev. Lett. **73**, 652 (1994).
[4] A. Melzer, T. Trittenberg, and A. Piel, Phys. Lett. A **191**, 301 (1994).
[5] Y. Hayashi and K. Tachibana, J. Vac. Sci. Technol. A **14**, 506 (1996).
[6] J. B. Pieper, J. Goree, and R. A. Quinn, J. Vac. Sci. Technol. A **14**, 519 (1996).
[7] H. Ikezi, Phys. Fluids **29**, 1764 (1986).
[8] E. B. Sirota, H. D. Ou-Yang, S. K. Sinha, P. M. Chaikin, J. D. Axe, and Y. Fujii, Phys. Rev. Lett. **62**, 1524 (1989).
[9] D. Hone, S. Alexander, P. M. Chaikin, and P. Pinkus, J. Chem. Phys. **79**, 1474 (1983)
[10] J. P. Hansen, Phys. Rev. A **8**, 3096 (1973); E. L. Pollock and J. P. Hansen, *ibid.* **8**, 3110 (1973).
[11] Lin I (private communication).
[12] It does not seem to follow always the direction of the confining walls.
[13] S. Vladimirov and M. Nambu, Phys. Rev. E **52**, R2172 (1995).
[14] F. Melandso and J. Goree, J. Vac. Sci. Technol. A **14**, 511 (1996).
[15] A. Melzer, V. A. Schweigert, I. V. Schweigert, A. Homann, S. Peters, and A. Piel, Phys. Rev. E **54**, R46 (1996); E. L. Pollock and J. P. Hansen, Phys. Rev. A **8**, 3110 (1973).
[16] M. S. Barnes, J. H. Keller, J. C. Forster, J. A. O'Neill, and D.

K. Coultas, Phys. Rev. Lett. **68**, 313 (1992).
[17] J. E. Daugherty, R. K. Porteous, M. D. Kilgore, and D. B. Graves, J. Appl. Phys. **72**, 3934 (1992).
[18] J. E. Daugherty, R. K. Porteous, and D. B. Graves, J. Appl. Phys. **73**, 7195 (1993).
[19] J. E. Daugherty, R. K. Porteous, and D. B. Graves, J. Appl. Phys. **73**, 1617 (1993).
[20] R. O. Rosenberg and D. Thirumalai, Phys. Rev. A **36**, 5690 (1987).
[21] M. O. Robbins, K. Kremer, and G. S. Grest, J. Chem. Phys. **88**, 3286 (1988); M. J. Stevens and M. O. Robbins, *ibid.* **98**, 2319 (1993).
[22] L. Foldy, Phys. Rev. A **3**, 3472 (1971).
[23] E. J. Meijer and D. Frenkel, J. Chem. Phys. **94**, 2269 (1991).
[24] R. T. Farouki and S. Hamaguchi, Appl. Phys. Lett. **61**, 2973 (1992); J. Chem. Phys. **101**, 9885 (1994); S. Hamaguchi and R. T. Farouki, *ibid.* **101**, 9876 (1994).
[25] Y. Rosenfeld, J. Chem. Phys. **103**, 9803 (1995).
[26] B. B. Laird and D. M. Kroll, Phys. Rev. A **42**, 4810 (1990).